THE JOURNAL OF
PHYSICAL CHEMISTRY C

Article

pubs.acs.org/JPCC

Physical Interpretation of Cyclic Voltammetry for Hybrid Pseudocapacitors

Henri-Louis Girard, Hainan Wang, Anna d'Entremont, and Laurent Pilon*

Henry Samueli School of Engineering and Applied Science, Mechanical and Aerospace Engineering Department, University of California Los Angeles, 420 Westwood Plaza, Los Angeles, California 90095, United States

S Supporting Information

ABSTRACT: This study aims to elucidate the respective contributions of faradaic reactions and electric double layer formation to charge storage in hybrid pseudocapacitors. It also aims to provide physical interpretation of experimental cyclic voltammetry (CV) measurements. First, a physicochemical transport model was derived from first-principles for simulating coupled interfacial, transport, and electrochemical phenomena in hybrid pseudocapacitors. The model simultaneously accounted for (i) charge transport in both electrodes and electrolyte, (ii) the dynamics of the electric double layer, (iii) steric repulsion due to finite ion sizes, (iv) redox reactions, and (v) intercalation. Then, CV curves were simulated for different electrode thicknesses and Li diffusion coefficients in the planar pseudocapacitive electrode. Particular attention was paid to the so-called *b*-value characterizing the power law evolution of the total current with respect to scan rate for a given potential. Overall, trends observed in numerically generated CV curves showed good agreement with experimental measurements. In addition, the results indicated that a *b*-value of unity across the potential window can be associated with purely faradaic charge storage with fast ion intercalation in the thin-film pseudocapacitive electrode. The study also demonstrates that under diffusion-limited conditions of Li intercalation in the pseudocapacitive electrode, the CV curves exhibited two distinct regimes: a faradaic regime dominated by faradaic reactions and a capacitive regime dominated by electric double layer formation. The *b*-value was near 1.0 in both regimes. However, a dip in the *b*-value, often observed experimentally, was also obtained and attributed to the transition between the capacitive and the faradaic regimes.

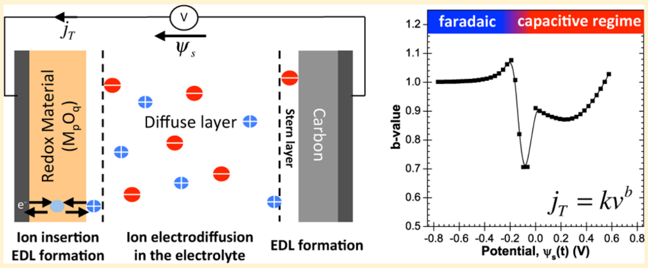

INTRODUCTION

Electrochemical capacitors, also known as supercapacitors, have attracted significant attention in recent years due to their promise as electrical energy storage devices for high energy and power applications.[1−3] They are typically classified as either electric double layer capacitors (EDLCs) or pseudocapacitors depending on the energy storage mechanism. EDLCs store energy physically in the electric double layers (EDLs) forming near the electrode/electrolyte interfaces.[1−3] Thus, the charge storage is highly reversible and the cycle life of EDLCs represents more than 100,000 cycles.[1] EDLCs are attractive for high power applications, such as in the regenerative braking system of hybrid electric vehicles as well as storing energy and balancing the load from intermittent renewable energy sources, due to their fast charging/discharging rates and long life.[1−4] However, the energy density of EDLCs remains low compared with that of batteries. Pseudocapacitors store energy via the electric double layers as well as via reversible oxidation−reduction (redox) reactions with or without insertion or intercalation.[1,3,5−7] Pseudocapacitors tend to feature larger capacitances and energy densities than EDLCs because the amount of charge they can store is not limited by the surface area of the electrode/electrolyte interface.[3,5−7] Finally, hybrid pseudocapacitors are devices combining a pseudocapacitive electrode made of a porous transition metal oxide (e.g., RuO_2, MnO_2, Nb_2O_5, MoO_3) and an EDLC-type electrode typically made of porous carbon.[2,8−12] These different devices hold great promise for meeting energy storage needs in current and emerging applications.[1−3,5−12]

In situ measurement of ion concentrations in the electrolyte and of intercalated species concentration profiles in the electrode during operation is very difficult, if not impossible. In addition, it is challenging to discriminate between the contributions of the redox reactions and of the EDL formation to the total current measured experimentally. This information can be obtained through physical modeling and simulations to improve the understanding of experimental measurements and to guide the optimization of the electrode and of the electrolyte.

This study aims to develop a physicochemical transport model for simulating hybrid pseudocapacitors under cyclic voltammetry by accurately accounting for interfacial and transport phenomena occurring in the electrolyte and for redox reactions and intercalation of the reaction product in the

Received: January 21, 2015
Revised: April 16, 2015
Published: May 4, 2015

DOI: 10.1021/acs.jpcc.5b00641
J. Phys. Chem. C 2015, 119, 11349−11361

pseudocapacitive electrode. This model was derived from first-principles in that it relies on the fundamental equations governing electrodynamics. It was used to elucidate the physical phenomena contributing to charge storage in pseudocapacitors and to provide physical interpretation of experimental measurements.

■ BACKGROUND

Electric Double Layer Structure. According to the Stern model, the electrolyte is divided into two domains: the Stern layer and the diffuse layer.[13] The Stern layer is a compact layer of charges adjacent to the electrode surface characterized by the absence of free charges. Within the diffuse layer, ions are free to move under the influence of diffusion, electromigration, and steric repulsion.[13] The thickness of the EDL can be approximated as the Debye length λ_D and varies with the diameters, valencies, and concentrations of ions as well as with temperature.[13]

Empirical Characterization of Pseudocapacitors. A semiempirical approach for analyzing cyclic voltammetry (CV) measurements has been developed and used extensively to characterize capacitive effects in the total current. Specifically, the measured total current density j_T at a given surface potential ψ_s was assumed to relate to the scan rate v according to the semiempirical relationship[14]

$$\frac{j_T(\psi_s)}{v^{1/2}} = k_1(\psi_s)\, v^{1/2} + k_2(\psi_s) \tag{1}$$

where $k_1(\psi_s)$ and $k_2(\psi_s)$ are semiempirical functions independent of v but dependent only on the cell potential ψ_s imposed between the current collectors. The functions $k_1(\psi_s)$ and $k_2(\psi_s)$ respectively correspond to the slope and intercept in the plot of $j_T/v^{1/2}$ versus $v^{1/2}$ for a given potential ψ_s.[14] This approach was supported by the facts that (i) the capacitive current j_C, associated with EDL formation or dissolution, is known to vary linearly with the scan rate v in the absence of redox reactions[13,15] and that (ii) the theoretical faradaic current j_F due to surface redox reactions in a semi-infinite electrolyte domain is proportional to $v^{1/2}$ when the presence of the EDL and the associated capacitive current are ignored.[13] This method has been used for full-cell hybrid pseudocapacitors with a chemically inert counter electrode[16] as well as for pseudocapacitors with Li or Na metal as the counter electrode to measure specifically the performance of the metal oxide electrode.[17−24] Furthermore, three-electrode experiments also used this approach to characterize pseudocapacitive electrodes.[7,14,25−31]

The presence of redox peaks in many pseudocapacitor CV curves shows that different processes can be dominant at different potentials. This led to another approach for analyzing experimental CV measurements. Assuming that the current at any potential is generally dominated by either a capacitive or a faradaic process, eq 1 can replaced by

$$j_T(\psi_s) = k(\psi_s)\, v^{b(\psi_s)} \tag{2}$$

where the exponent $b(\psi_s)$ is the so-called b-value expected to vary between $b = 1/2$ in the case of purely faradaic current and $b = 1$ for purely capacitive current.[14,25] The value of b is typically evaluated by least-squares fitting of $j_T(\psi_s)$ versus v for given values of ψ_s.[14,25] A b-value of 1 corresponds to a greater rate capability and is therefore desirable for all potentials in the operating window. It has been attributed to "capacitive current"[14,25] or described more cautiously as "capacitive behavior",[22,31,32] as "pseudocapacitive behavior",[20,21] or as "non-diffusion controlled charge storage".[28] In addition, a dip is often observed in the b-value plotted as a function of ψ_s.[18,25,28] This has been attributed to the presence of redox peaks from the faradaic reaction in the CV curves.[18,25,28] To the best of our knowledge, despite its extensive usage, this semiempirical analysis and its physical interpretation have not been rigorously demonstrated, particularly for simultaneous electric double layer formation, redox reactions, and ion insertion in the pseudocapacitive electrode.

Models of Pseudocapacitors. A variety of models for pseudocapacitors have been proposed. Equivalent RC circuit and transmission line models consist of modeling a physical device by a succession of ideal capacitors and resistors integrated in a circuit.[33] They have been used to study the charging/discharging dynamics of pseudocapacitors.[33−35] However, these models have to be fitted with experimental data to retrieve the values of the different resistances and capacitances.[35] They can be used to control the device operation, but they cannot be used to design the electrodes or electrolyte of novel pseudocapacitors. Moreover, the classical RC circuit models neglect ion diffusion and nonuniform ion concentration in the electrolyte.[36] As faradaic reactions depend strongly on the ion concentrations at the reaction plane, these models are therefore not suitable for modeling pseudocapacitors with simultaneous faradaic and capacitive currents.

Continuum models, numerically solving the Poisson equation for electric field and the mass conservation equations for ion concentrations, have also been developed to analyze pseudocapacitors.[37−45] Different approaches investigated the effects of porosity,[46] redox-active particle size,[37−39,42] solid phase diffusion limitation in the case of ion intercalation,[42] and moving reaction fronts.[40] However, these models imposed the double layer areal capacitance (in F/m^2) or volumetric capacitance (in F/m^3) as constant properties independent of the electric potential instead of predicting them.[37−46] Unfortunately, the double layer capacitance is known to vary nonlinearly with electric potential under large electric potentials and electrolyte concentrations.[47] Furthermore, some models assumed the concentration of ions at the reaction front in the electrolyte was the bulk concentration[37,39,40,44,46] although the electric field and the presence of EDLs near the electrodes affect the concentrations of the ions involved in the faradaic reaction.

Finally, first-principles molecular dynamics (MD) simulations have been performed to explore the fundamental electrochemical behaviors of pseudocapacitive materials including RuO_2,[48,49] TiO_2,[50] MnO_2,[51] and MoO_3.[52] However, the computational complexity and cost limit MD simulations to extremely small time and length scales on the order of 10 ns and 10 nm, respectively.[48,53] These are significantly smaller than those encountered in actual characterization methods such as cyclic voltammetry or galvanostatic cycling, which are on the order of several micrometers and seconds.[7,8] For example, He et al.[54] simulated cyclic voltammetry for two cylindrical pores with subnanometer width at unrealistically large scan rates of 1 to 10 MV/s to study the local dynamics of charging and discharging. Because of the small time and length scales, such studies cannot simulate relatively slow and long-range diffusion processes across an electrode. Therefore, MD simulations seem inadequate for reproducing experimental cycling with realistic time scales for electrodes or devices with realistic dimensions.

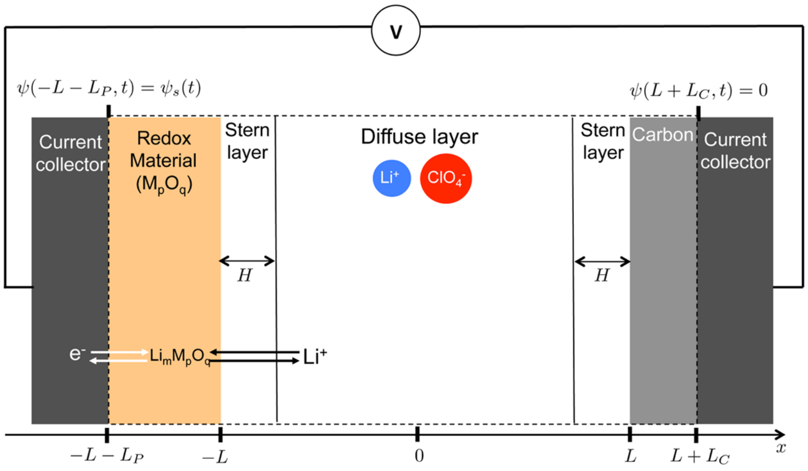

Figure 1. Schematic of the simulated one-dimensional hybrid pseudocapacitor cell consisting of a redox-active pseudocapacitive electrode and a carbon electrode with $LiClO_4$ electrolyte in PC. The dashed line encloses the computational domain simulated.

This study aims to develop a continuum model to accurately simulate coupled interfacial, transport, and electrochemical phenomena in hybrid pseudocapacitors subjected to cyclic voltammetry. The model simultaneously accounted for (i) charge transport in both electrodes and electrolyte, (ii) the dynamics of the electric double layer, (iii) steric repulsion due to finite ion sizes, (iv) redox reactions, and (v) ion intercalation in the pseudocapacitive electrode. The goal of this study is also to rigorously examine the respective contributions of capacitive and faradaic current densities to the total current density and provide physical interpretations of experimentally obtained CV curves. Finally, it aims to assess whether $b = 1$ in eq 2 can be associated with faradaic reactions and why a dip is often observed in the b-value versus potential plot.[18,25,28]

■ ANALYSIS

Schematics and Assumptions. Figure 1 shows the schematic of the one-dimensional hybrid pseudocapacitor simulated as well as the associated computational domain and coordinate system. The cell consisted of a planar thin-film pseudocapacitive electrode made of transition metal oxide M_pO_q of thickness L_P and a planar carbon electrode of thickness L_C. They were separated by an electrolyte of thickness $2L$ made of $LiClO_4$ salt in propylene carbonate (PC) solvent. The electrolyte domain was divided in three regions corresponding to a Stern layer of thickness H near each electrode surface and a diffuse layer beyond. This simplified geometry was chosen in order to assess the contribution of multiple and closely coupled physical phenomena in detail without considering the multidimensional nature of actual electrodes. Note also that the electrode curvature was found to have negligible effect on the areal capacitance of an EDL on a sphere of radii larger than 40 nm.[55] The following reversible redox reaction was assumed to take place at the pseudocapacitive electrode

$$m\mathrm{Li}^+ + \mathrm{M}_p\mathrm{O}_q + me^- \rightleftharpoons \mathrm{Li}_m\mathrm{M}_p\mathrm{O}_q \tag{3}$$

To make the problem mathematically tractable, the following assumptions were made: (1) electrodiffusion of Li^+ and ClO_4^- ions in the electrolyte and insertion (or intercalation) of Li atoms in the electrode were one-dimensional. (2) The Stern layer thickness H was approximated as the radius of the largest solvated ion species, namely, ClO_4^-, so that $H = a_2/2$.[13,56,57] In practice, the ions may lose part or all of their solvation shell as they approach the electrode. Therefore, the solvated ion diameter may depend on the location considered.[58] However, to the best of our knowledge, no quantitative model exists relating the partially solvated ion diameter to the local electric field and position with respect to the electrode. (3) The diffusion coefficients of all ion species in the electrolyte and that of Li in the redox-active electrode were independent of their respective concentrations. Their values corresponded to those of dilute solutions reported in the literature. Note that in reality the ion diffusion coefficients vary with ion concentration. Umino and Newman[59] reported that the diffusion coefficient of H^+ and SO_4^{2-} for H_2SO_4 in water varied nonlinearly with salt concentration. However, it did not exceed 40% of its asymptotic value corresponding to dilute solutions for concentrations ranging from 0.3 to 7.5 M. In fact, it was verified numerically that accounting for concentration-dependent diffusion coefficient had a negligible impact on the predicted current at the scan rates considered in this study when ion diffusion in the electrolyte was not limiting (see Supporting Information). (4) Isothermal conditions prevailed throughout the device. (5) Advection in the electrolyte was negligible. (6) The reversible redox reaction given by eq 3 was heterogeneous and occurred at the electrode/electrolyte interface near the pseudocapacitive electrode at $x = -L + H$.[13] This assumption is commonly used in modeling battery and supercapacitor,[13] as free electrons are assumed to be confined in the electrode and free Li^+ ions are confined in the electrolyte. (7) The intercalation and deintercalation of Li atoms into and out of the pseudocapacitive electrode were treated as diffusion processes. (8) The redox-active material did not undergo any phase transition. This assumption is consistent with observations on Nb_2O_5 thin films during lithium insertion.[60] (9) The electrical conductivity σ_P and the Li diffusion coefficient $D_{1,P}$ of the pseudocapacitive electrode were constant. In practice, they may change with Li insertion. However, to the best of our knowledge, no quantitative model or experimental measurements exist capturing these effects in a thin film of metal oxide. (10) The specific ion adsorption due to nonelectrostatic forces was assumed to be negligible. Note that previous simulations of EDLCs based on this assumption agreed well with experimental data.[61,62] (11) The potential drop across the highly conducting current collectors was negligible so that only the electrodes and electrolyte domains were simulated. The goal of this study is to reproduce trends in CV curves and to provide physical interpretation of behaviors observed experimentally. The assumptions considered have been widely used in the literature to make possible simulations of pseudocapacitors.

Governing Equations. The local electric potential $\psi\,(x,\,t)$ in the pseudocapacitive ($-L_P - L \leq x \leq -L$) and carbon ($L \leq x \leq L + L_C$) electrodes is governed by the one-dimensional Poisson equation expressed as[56,63]

$$\frac{\partial}{\partial x}\left(\sigma_P \frac{\partial \psi}{\partial x}\right) = 0 \quad \text{in the pseudocapacitive electrode} \tag{4}$$

$$\frac{\partial}{\partial x}\left(\sigma_C \frac{\partial \psi}{\partial x}\right) = 0 \quad \text{in the carbon electrode} \tag{5}$$

where σ_P and σ_C are the electrical conductivities of the pseudocapacitive and carbon electrode, respectively.

The local molar concentration of intercalated Li atoms in the pseudocapacitive electrode, denoted by $c_{1,P}(x,t)$, is governed by the mass diffusion equation given by[63,64]

$$\frac{\partial c_{1,P}}{\partial t} = \frac{\partial}{\partial x}\left(D_{1,P} \frac{\partial c_{1,P}}{\partial x}\right) \quad \text{in the pseudocapacitive electrode} \tag{6}$$

where $D_{1,P}$ is the diffusion coefficient of intercalated lithium atoms in the pseudocapacitive electrode.

Moreover, the potential and ion concentrations in the diffuse layer of the electrolyte solution ($-L + H \leq x \leq L - H$) are governed by the generalized modified Poisson−Nernst−Planck (GMPNP) model derived by Wang et al.[56] The GMPNP model was developed for asymmetric electrolytes with multiple ions species of finite size. For binary and asymmetric electrolytes the GMPNP in the diffuse layer is expressed as[56]

$$\begin{cases} \dfrac{\partial}{\partial x}\left(\epsilon_0 \epsilon_r \dfrac{\partial \psi}{\partial x}\right) = -F \displaystyle\sum_{i=1}^{2} z_i c_i & \text{(7a)} \\ \dfrac{\partial c_i}{\partial t} = -\dfrac{\partial N_i}{\partial x} \quad \text{for } i = 1,\, 2 & \text{(7b)} \end{cases}$$

where $c_i(x,t)$ is the local molar concentration of ion species i in the electrolyte solution at time t. Here, $i = 1$ refers to Li^+ and $i = 2$ refers to $\mathrm{ClO_4}^-$. Moreover, $F = 96\,485$ C mol^{-1} is the Faraday constant, $\epsilon_0 = 8.854 \times 10^{-12}$ F m^{-1} is the free space permittivity, and ϵ_r is the relative permittivity of the electrolyte solution. The local mass flux of ion species i, denoted by $N_i(x,t)$ in mol m^{-2} s^{-1}, is defined for a binary and asymmetric electrolyte as[56]

$$N_i(x,\,t) = -D_i \frac{\partial c_i}{\partial x} - \frac{D_i F z_i c_i}{R_u T} \frac{\partial \psi}{\partial x} - \frac{D_i c_i}{1 - \sum_{j=1}^{2} c_j / c_{j,max}} \frac{\partial}{\partial x}\left(\sum_{j=1}^{2} c_j / c_{j,max}\right) \tag{8}$$

where D_i and a_i are the diffusion coefficient and the effective ion diameter of ion species i in the electrolyte solution, respectively. The temperature is denoted by T (in K), while $N_A = 6.022 \times 10^{23}$ mol^{-1} and $R_u = 8.314$ J K^{-1} mol^{-1} are the Avogadro constant and the universal gas constant, respectively. The maximum concentration $c_{j,max} = 1/(N_A\, a_j^3)$ corresponds to simple cubic ion packing at the electrode surface. The first and second terms of eq 8 represent the ion flux due to diffusion and electromigration, respectively, while the last term represents a correction accounting for finite ion size.[56] Finally, the presence of the Stern layers near each electrode was accounted for via boundary conditions,[56,62] and no governing equations for $\psi(x,t)$ and $c_i(x,t)$ needed to be formulated or solved within the Stern layer.

Boundary and Initial Conditions. The one-dimensional governing eqs 4 to 8 are second-order partial differential equations in space and first-order in time. Each equation requires two boundary conditions and one initial condition in each region it is solved.

First, the initial electric potential was assumed to be uniform across the device and given by

$$\psi(x,\,0) = 0 \text{ V} \tag{9}$$

Initially, the Li^+ and $\mathrm{ClO_4}^-$ ion concentrations in the electrolyte ($-L + H \leq x \leq L - H$) were taken as uniform and equal to their bulk concentrations satisfying electroneutrality according to

$$c_1(x,\,0) = c_{1,\infty} \quad \text{and} \quad c_2(x,\,0) = -z_1 c_{1,\infty}/z_2 \tag{10}$$

Similarly, the initial Li concentration in the pseudocapacitive electrode ($-L - L_P \leq x \leq -L$) was uniform and equal to $c_{1,P,0}$, i.e.

$$c_{1,P}(x,\,0) = c_{1,P,0} \tag{11}$$

The potential at the current collector/pseudocapacitive electrode interface was imposed as $\psi(-L - L_P,t) = \psi_s(t)$. During cyclic voltammetry measurements, $\psi_s(t)$ varied linearly with time according to[56]

$$\psi_s(t) = \begin{cases} \psi_{\max} - v[t - (n_c - 1)\tau_{CV}] \\ \quad \text{for } (n_c - 1)\tau_{CV} \leq t < (n_c - 1/2)\tau_{CV} \\ \psi_{\min} + v[t - (n_c - 1/2)\tau_{CV}] \\ \quad \text{for } (n_c - 1/2)\tau_{CV} \leq t < \ n_c\ \tau_{CV} \end{cases} \tag{12}$$

where n_c is the cycle number and τ_{CV} is the cycle period, while ψ_{max} and ψ_{min} are the maximum and minimum values of the cell potential $\psi_s(t)$, respectively. In addition, the carbon electrode surface was electrically grounded so that $\psi(L + L_C,t) = 0$ V. Note that the choice of electrical ground is arbitrary and was made for convenience. It did not affect the predicted CV curves or the associated physical interpretations.

The electric potential varied linearly across the Stern layers so that the electric fields at the pseudocapacitive and carbon electrodes satisfied[56,62]

$$-\frac{\partial \psi}{\partial x}(-L + H,\, t) = \frac{1}{H}[\psi(-L,\, t) - \psi(-L + H,\, t)] \tag{13a}$$

$$\frac{\partial \psi}{\partial x}(L - H,\, t) = \frac{1}{H}[\psi(L,\, t) - \psi(L - H,\, t)] \tag{13b}$$

These boundary conditions accounted for the presence of the Stern layers at both electrodes without explicitly simulating them in the computational domain.[62]

The current density at the pseudocapacitive electrode/electrolyte interface, located at $x = -L$ was equal to the sum of the capacitive $j_C(x,t)$ and faradaic $j_F(t)$ current densities (in

A/m^2) at the Stern/diffuse layer interface, located at $x = -L + H$, so that[56,65]

$$-\sigma_P \frac{\partial \psi}{\partial x}(-L, t) = j_C(-L + H, t) + j_F(t) \tag{14}$$

However, near the carbon electrode at $x = +L$, only the capacitive current contributed to the total current density so that

$$-\sigma_C \frac{\partial \psi}{\partial x}(L, t) = j_C(L - H, t) \tag{15}$$

In both cases, $j_C(x,t)$ is the displacement current density due to the electric double layer formation at the pseudocapacitive and carbon electrodes and defined as[66]

$$j_C(\pm(L - H), t) = -\epsilon_0 \epsilon_r \frac{\partial^2 \psi}{\partial x \partial t}(\pm(L - H), t) \tag{16}$$

In addition, the faradaic current density $j_F(t)$ is typically described by the generalized Frumkin−Butler−Volmer model evaluated at the pseudocapacitive electrode/electrolyte interface and expressed as[13]

$$j_F(t) = j_{F,0}(t)\left\{\exp\left[\frac{(1-\alpha) z_1 F \eta}{R_u T}\right] - \exp\left[\frac{-\alpha z_1 F \eta}{R_u T}\right]\right\} \tag{17}$$

where $\eta(t) = \Delta\psi_H(t) - \Delta\psi_{eq}$ is the overpotential and $\Delta\psi_H(t) = \psi(-L,t) - \psi(-L+H,t)$ is the electrical potential drop across the Stern layer near the pseudocapacitive electrode.[13] For electrodes made of transition metal oxides, the equilibrium potential difference $\Delta\psi_{eq}$ is typically fitted experimentally as a function of the state-of-charge $c_{1,P}/c_{1,P,max}$, where $c_{1,P,max}$ is the maximum concentration of intercalated lithium atoms in the pseudocapacitive electrode.[42,45,67] It can be obtained by fitting experimental data for the open-circuit potential.[63,65] The so-called exchange current density $j_{F,0}(t)$ can be written as[63,65]

$$j_{F,0}(t) = F z_1 k_0 [c_1(-L + H, t)]^{1-\alpha} [c_{1,P,max} - c_{1,P}(-L, t)]^{\alpha} [c_{1,P}(-L, t)]^{\alpha} \tag{18}$$

where k_0 is the reaction rate constant expressed in m$^{1+3\alpha}$ mol$^{-\alpha}$ s^{-1}. Here, the transfer coefficient α was assumed to be 0.5, corresponding to identical energy barriers for forward and backward redox reactions.[13] In this case, the faradaic current $j_F(t)$ has the same sign as the overpotential $\eta(t)$.

Moreover, the current collector was impermeable to the lithium atoms intercalated in the pseudocapacitive electrode so that the mass flux of Li vanished at the pseudocapacitive electrode/current collector interface, i.e.

$$-D_{1,P} \frac{\partial c_{1,P}}{\partial x}(-L - L_P, t) = 0 \text{ mol m}^{-2}\text{ s}^{-1} \tag{19}$$

The mass flux of Li exiting through the pseudocapacitive electrode/electrolyte interface was related to the faradaic current density $j_F(t)$ based on stoichiometry as

$$-D_{1,P} \frac{\partial c_{1,P}}{\partial x}(-L, t) = \frac{j_F(t)}{z_1 F} \tag{20}$$

The mass flux of Li$^+$ ions ($i = 1$) across the Stern/diffuse layer interface near the pseudocapacitive electrode was related to $j_F(t)$ in the same way, while it vanished near the carbon electrode such that

$$N_1(-L + H, t) = \frac{j_F(t)}{z_1 F} \quad \text{and} \quad N_1(L - H, t) = 0 \text{ mol m}^{-2}\text{ s}^{-1} \tag{21}$$

Both the carbon and pseudocapacitive electrodes were impermeable to ClO_4^- ions ($i = 2$) so that

$$N_2(-L + H, t) = N_2(L - H, t) = 0 \text{ mol m}^{-2}\text{ s}^{-1} \tag{22}$$

Finally, the present model can be extended to pseudocapacitors with two redox-active electrodes by adding the corresponding faradaic current j_F at the Stern/diffuse layer interface near the counter electrode ($x = L - H$) and solving the mass conservation equation for intercalated Li in both electrodes. However, current symmetric pseudocapacitors have been shown to have numerous limitations, including lower gravimetric energy and power densities[68] and smaller potential window due to irreversible redox reactions occurring at one of the electrodes.[68] Hybrid pseudocapacitors enable better control of the intercalation reaction in the pseudocapacitive electrode and feature better overall performance.[69]

Constitutive Relationships. A total of 23 input parameters were needed to solve eqs 4 to 22 including (i) the electrolyte properties $\epsilon_r(0)$, β, n, a_1, a_2, z_1, z_2, D_1, D_2, and $c_{1,\infty}$, (ii) the pseudocapacitive electrode properties σ_P, $D_{1,P}$, $c_{1,P,0}$, k_0, and $\Delta\psi_{eq}$, (iii) the carbon electrode conductivity σ_C, (iv) the cell dimensions L, L_P, and L_C, and (v) the operating conditions T, ψ_{max}, ψ_{min}, and v. Typical values were collected from the literature.

The electrolyte considered in the present study was $LiClO_4$ in the organic solvent propylene carbonate (PC) at $T = 298$ K. The relative permittivity of the electrolyte ϵ_r is known to decrease significantly at large electric fields due to the saturation of the polarization of the solvent molecules. The Booth Model has been developed to account for this effect and is expressed as[70,71]

$$\epsilon_r(E) = n^2 + (\epsilon_r(0) - n^2)\frac{3}{\beta E}\left[\coth(\beta E) - \frac{1}{\beta E}\right] \tag{23}$$

where E is the norm of the local electric field, $\epsilon_r(0)$ is the relative permittivity at zero electric field, n is the index of refraction of the electrolyte at zero electric field, and β is an empirically defined fitting parameter. For propylene carbonate, these parameters are as follows $\epsilon_r(0) = 64.4$, $n = 1.42$, and $\beta = 1.314 \times 10^{-8}$ m/V.[61] The effective solvated ion diameters of Li$^+$ ($z_1 = +1$) and ClO_4^- ($z_2 = -1$) in PC were taken as $a_1 = 0.67$ nm and $a_2 = 1.0$ nm, respectively.[72] The Stern layer thickness H, corresponding to the distance of closest approach to the electrode plane, was equal to the largest solvated ion radius, i.e., $H = a_2/2 = 0.5$ nm.[56] The ion diffusion coefficients of Li$^+$ and ClO_4^- in PC were taken as $D_1 = 2.6 \times 10^{-10}$ m^2/s and $D_2 = 3.3 \times 10^{-10}$ m^2/s, respectively.[72] The initial bulk ion concentrations were imposed as $c_{1,\infty} = c_{2,\infty} = 1$ mol/L, typical of electrochemical capacitors.[18,20,73]

The pseudocapacitive electrode properties were inspired by those of Nb_2O_5 whenever available since Nb_2O_5 was shown to be a good material for intercalation pseudocapacitance.[74] The electrical conductivity of metal oxides may increase with the amount of intercalated lithium.[75] Here, however, a constant value $\sigma_P = 10^{-5}$ S/m was selected based on the range of lithium concentration observed.[76] The electrical conductivity of the carbon electrode was taken as $\sigma_C = 5$ S/m corresponding to

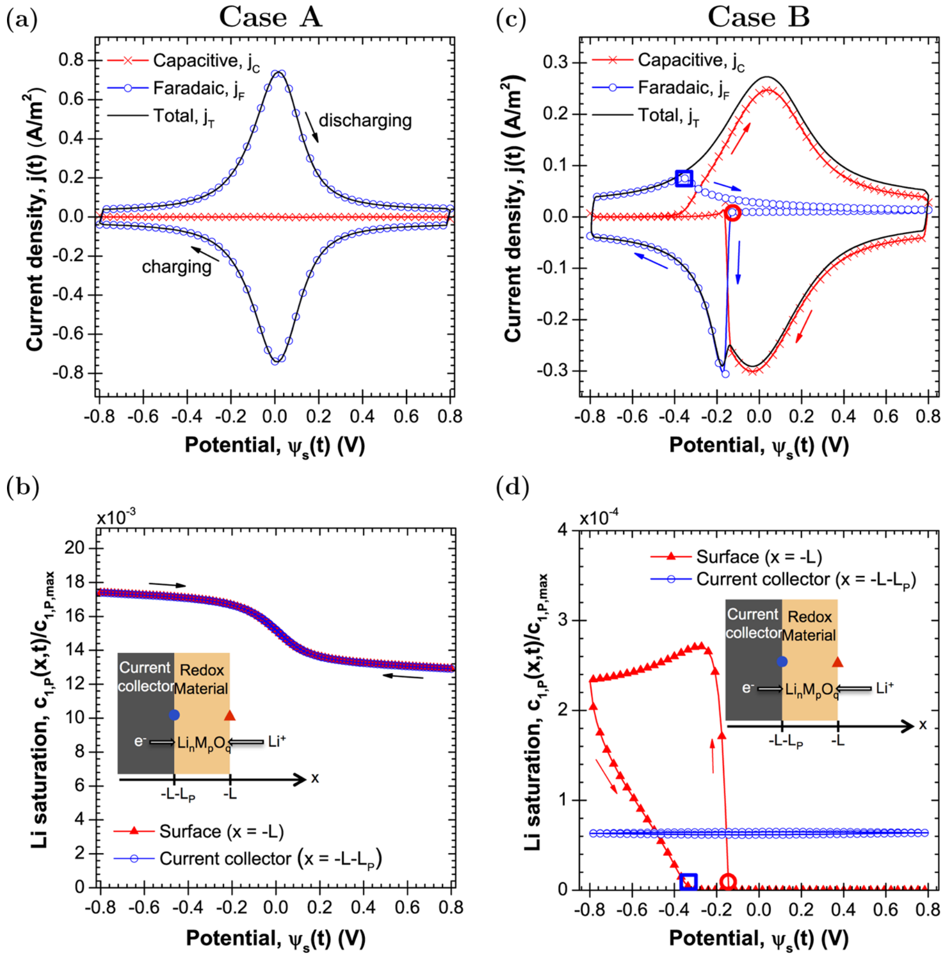

Figure 2. Top: Capacitive j_C, faradaic j_F, and total j_T current densities versus cell potential ψ_s for a scan rate $\nu = 1$ V/s for (a) Case A and (c) Case B. Bottom: Intercalated lithium concentration normalized by the maximum concentration at the pseudocapacitive electrode surface ($x = -L$) and at the current collector ($x = -L - L_P$) for (b) Case A and (d) Case B at scan rate $\nu = 1$ V/s. The red circle and blue square are guides corresponding to the same instant in the cycle in figures panels c and d.

that of activated carbon.[77] The reaction rate constant k_0 for transition metal oxides has been reported to range between 10^{-11} and 10^{-8} m$^{2.5}$ mol$^{-0.5}$ s^{-1}.[63,65,78] Its value was taken as $k_0 = 10^{-8}$ m$^{2.5}$ mol$^{-0.5}$ s^{-1}, i.e., the most favorable redox reaction condition. In addition, the equilibrium potential difference $\Delta\psi_{eq}$ was assumed to be constant and equal to zero for the sake of simplicity.[79] Note that, in reality, the equilibrium potential difference varies linearly with the state of charge $c_{1,P}/c_{1,P,max}$ of the electrode.[34] We verified that in all cases considered here, the variation of $\Delta\psi_{eq}$ did not affect the current magnitude or the b-value (see Supporting Information). The maximum intercalated lithium concentration in the redox active electrode was estimated as $c_{1,P,max} = m\rho/M$ where ρ and M are the density and molar mass of the fully intercalated metal oxide. For $Li_2Nb_2O_5$, ρ and M were reported as $\rho \approx 4.6$ g/cm^3 and $M = 279.7$ g/mol[42] yielding $c_{1,P,max} \approx 32.9$ mol/L. The diffusion coefficient $D_{1,P}$ of intercalated lithium atoms in transition metal oxides typically ranges from 10^{-16} to 10^{-10} m^2/s.[78] Here, it will be treated as a variable parameter to explore asymptotic behaviors of hybrid pseudocapacitors. Finally, the initial concentration of Li in the electrode $c_{1,P,0}$ was adjusted on a case by case basis. First, imposing $c_{1,P,0} = 0$ mol/L initially would prevent any faradaic current $j_F(t)$ [eq 18] and ion insertion at any later time. Similarly, if $c_{1,P,0}$ is too low during the first deintercalation step, the Li concentration in the electrode may reach zero resulting in the absence of faradaic current at any subsequent time. However, it is important to note that the choice of a sufficiently large value of $c_{1,P,0}$ had no effect on the oscillatory steady state solution. Note also that some metal oxide electrode synthesis processes result in electrodes preloaded with Li atoms.[80]

Moreover, the electrolyte thickness was taken as $2L = 2$ μm, while the electrode thicknesses L_P and L_C were identical and equal to either 20 or 500 nm. The potential window was selected to be large enough to show all relevant phenomena occurring during charging and discharging. Consequently, the pseudocapacitive electrode potential was cycled between −0.8 and +0.8 V, while the carbon electrode was grounded. Finally, the scan rate ν was arbitrarily varied from 10^{-2} to 10 V/s. The scan rate values were large compared with those used experimentally due to the fact that diffusion limitation occurs at a much higher scan rate for the simulated planar electrodes than for actual porous electrodes. The scan rate was chosen to explore these effects. In addition, simulations with relatively large scan rate took less time and reached an oscillatory steady state faster.

Method of Solution and Data Processing. The governing eqs 4 to 8 were solved along with the boundary and initial conditions given by eqs 9 to 22 using the commercial finite element solver COMSOL 4.3b running in parallel on 8 cores with 64 GB of RAM. The numerical convergence criterion was defined such that the maximum relative difference in the predicted current densities j_C and j_F at the Stern/diffuse layer interface near the pseudocapacitive electrode ($x = -L + H$) was less than 1% when dividing both the mesh size and the time step by a factor of two. This corresponded to imposing a time step of $\Delta t \approx \tau_{CV}/1000 = (\psi_{max} - \psi_{min})/1000v$. The mesh size was the smallest at the Stern/diffuse layer interface due to the large potential gradient and gradually increased away from the electrode. The mesh size was specified to be less than 0.025 nm at the Stern/diffuse layer interface, while it was less than $L_P/25$ and $L_C/25$ in the electrode domains and less than $L/50$ in the diffuse layer. The total number of finite elements was about 500 for all cases simulated in the present study. The criterion for reaching oscillatory steady state was similar when running an additional 10 cycles. This corresponded to running 10 cycles for each case studied.

The instantaneous total current density $j_T(t)$ at the pseudocapacitive electrode/electrolyte interface was computed as the sum $j_T(t) = j_C(t) + j_F(t)$ where the capacitive $j_C(t)$ and faradaic $j_F(t)$ current densities were given by eqs 16 and 17, respectively. CV curves at a specific scan rate were obtained by plotting $j_T(t)$, $j_C(t)$, and $j_F(t)$ as functions of $\psi_s(t)$. Finally, the areal integral capacitance $C_{s,int}$ (in F/cm^2) was computed from the total current $j_T(t)$ and the imposed potential $\psi_s(t)$ according to[81]

$$C_{s,int} = \frac{1}{\psi_{\max} - \psi_{\min}} \oint \frac{j_T(\psi_s)}{2v} \, d\psi_s \qquad (24)$$

RESULTS AND DISCUSSION

General CV Curve Behavior. To study the effects of the pseudocapacitive electrode properties on the performance of a hybrid pseudocapacitor, two extreme cases were defined. First, Case A corresponded to a thin-film pseudocapacitive electrode with fast Li intercalation such that $L_P = 20$ nm and $D_{1,P} = 10^{-10}$ m^2/s. Case B corresponded to a thick pseudocapacitive electrode with slow Li intercalation so that $L_P = 500$ nm and $D_{1,P} = 10^{-14}$ m^2/s. These electrode thicknesses are representative of actual pseudocapacitive nanoparticles on a conductive substrate[25] and thick film coating or microspheres,[82] respectively. Additionally, the values of the diffusion coefficient $D_{1,P}$ was selected such that in Case A, the diffusion length L_D defined as $L_D = (D_{1,P}\,\tau_{CV}/2)^{1/2} = 12.6$ μm was significantly larger than the electrode thickness, whereas in Case B, the diffusion length $L_D = 126$ nm was on the order of the electrode thickness. Thus, these parameters were chosen as extreme values to explore both the lithium diffusion limited and the diffusion-independent regimes in the pseudocapacitive electrode. The diffusion coefficient of Li in a metal oxide electrode would typically increase with the concentration of intercalated Li. However, to the best of our knowledge, no model capturing this effect is available. Therefore, the values were selected arbitrarily within a reasonable range to explore asymptotic behaviors. Other input parameters were identical for both cases and given in Constitutive Relationships. In both Cases A and B, charging corresponded to reduction of Li$^+$ ions into Li atoms, which intercalated into the redox-active electrode. Discharging corresponded to deintercalation and oxidation of Li atoms into Li$^+$ ions that diffused in the electrolyte.

Figure 2a shows the predicted capacitive j_C, faradaic j_F, and total j_T current densities for Case A under oscillatory steady state as functions of the imposed potential $\psi_s(t)$ for scan rate $v = 1$ V/s. The CV curve j_T vs ψ_s featured a peak in both charging, for decreasing ψ_s, and discharging, for increasing ψ_s, currents around $\psi_s = 0$ V. Figure 2a also shows that the faradaic current dominated during the entire cycle and the capacitive current was negligible. This can be attributed to fast redox reactions and intercalation of Li atoms in the thin electrode. Indeed, the large reaction rate guaranteed that Li$^+$ ions at the Stern/diffuse layer interface were consumed by the redox reaction during charging. In addition, the large diffusion coefficient of Li$^+$ ions in the electrolyte ensured sufficient supply of Li$^+$ during charging. Similarly, the large diffusion coefficient of Li in the pseudocapacitive electrode ensured sufficient supply of Li atoms to be oxidized at the electrode/electrolyte interface during discharging. Then, no significant capacitive current resulting from EDL formation was observed.

Figure 2b shows the intercalated lithium saturation in the redox-active electrode as a function of $\psi_s(t)$ defined (i) at the electrode/current collector interface as $c_{1,P}(-L - L_P,t)/c_{1,P,max}$ and (ii) at the electrode/electrolyte interface as $c_{1,P}(-L,t)/c_{1,P,max}$. First, the two curves were superimposed indicating that the concentration of intercalated Li was uniform throughout the pseudocapacitive electrode. This was verified by plotting the concentration profile in the electrode. Second, neither curve shows any hysteresis during the entire cycle. This can be attributed to the fast intercalation and deintercalation and to the small electrode thickness, which did not limit the redox reactions.

Figure 2c shows the current densities j_C, j_F, and j_T predicted for Case B under oscillatory steady state as functions of potential $\psi_s(t)$ ranging between −0.8 and 0.8 V for a scan rate v of 1 V/s. In contrast to Case A (Figure 2a), Figure 2c shows that, for slow Li diffusion in a thick electrode, the faradaic current j_F dominated only in the lower end of the potential window, while the capacitive current j_C dominated in the higher end during both charging and discharging. In addition, the total current j_T and the integral capacitance were smaller in Case B than in Case A for the same $v = 1$ V/s. In Case B, the CV curve featured three peaks in the total current: at $\psi_s = 0$ V in both the charging and the discharging phase, and at $\psi_s = -0.15$ V in the charging phase. Figure 2d shows the intercalated lithium saturation in the redox active electrode as a function of $\psi_s(t)$ (i) at the electrode/current collector interface $c_{1,P}(-L - L_P,t)/c_{1,P,max}$ and (ii) at the electrode/electrolyte interface $c_{1,P}(-L,t)/c_{1,P,max}$. At the current collector/electrode interface, the saturation $c_{1,P}(-L - L_P,t)/c_{1,P,max}$ remained constant throughout the entire cycle. Indeed, the low diffusion coefficient $D_{1,P}$ and the thick electrode prevented the intercalated lithium from reaching the current collector before the current was reversed. Note, however, that the value of $c_{1,P}(-L - L_P,t)$ was different from its initial value $c_{1,P,0}$. During charging, the saturation $c_{1,P}(-L,t)/c_{1,P,max}$ at the electrode/electrolyte interface increased sharply at potential $\psi_s \approx -0.15$ V corresponding to the sudden increase in the faradaic current reaching a peak at −0.15 V, as observed in Figure 2c (red circle). During discharging, the saturation at the pseudocapacitive electrode/electrolyte interface reached zero around $\psi_s = -0.3$ V corresponding to the steep drop observed in the faradaic current j_F in Figure 2c (blue square). Then, $c_{1,P}(-L,t)/c_{1,P,max}$ was very small, and the faradaic current was limited by the diffusion of Li out of the pseudocapacitive electrode. Note

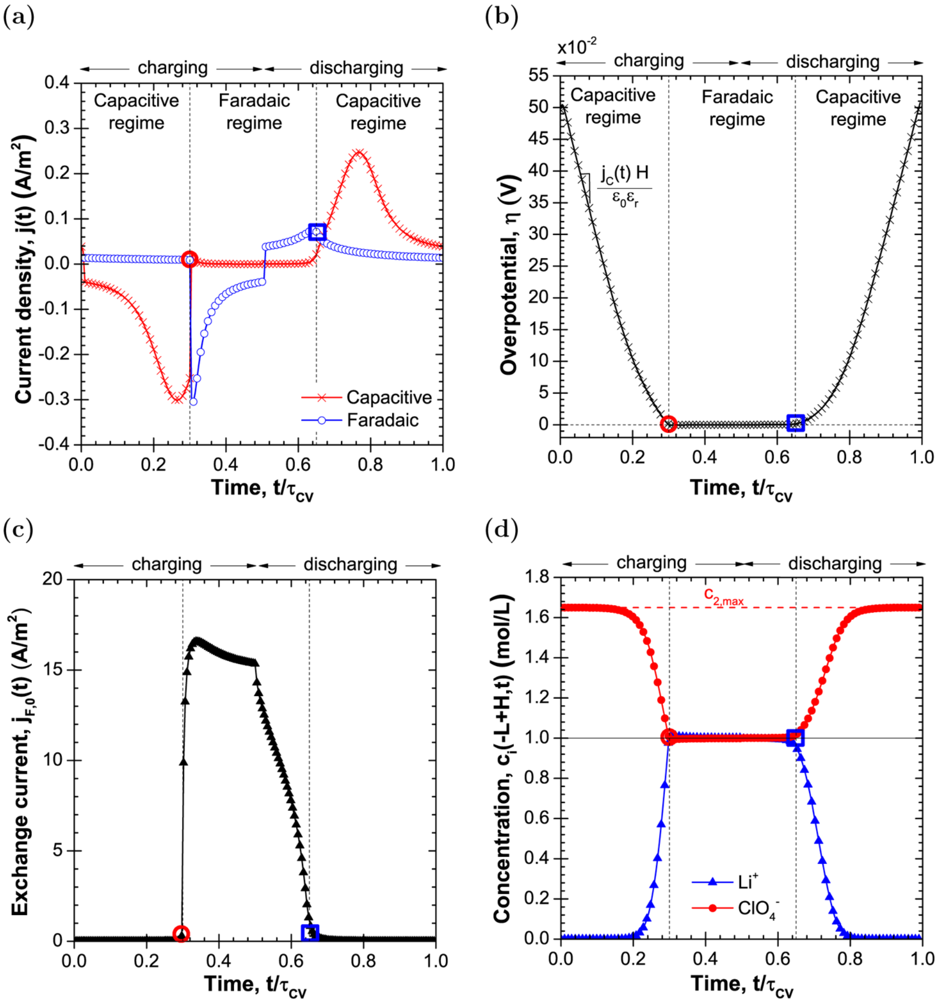

Figure 3. Temporal evolution of (a) the faradaic $j_F(t)$ and capacitive $j_C(t)$ current densities, (b) the overpotential $\eta(t)$, (c) the exchange current density $j_{F,0}(t)$, and (d) the ion concentrations $c_1(-L + H,t)$ of Li^+ and $c_2(-L + H,t)$ of ClO_4^- at the Stern/diffuse layer interface near the pseudocapacitive electrode as functions of dimensionless time t/τ_{CV} for Case B at scan rate $v = 1$ V/s. Here, the vertical dashed lines indicate transitions at $t/\tau_{CV} = 0.3$ ($\psi_s = -0.15$ V) and $t/\tau_{CV} = 0.65$ ($\psi_s = -0.3$ V). The red circle and blue square correspond to the identical indicators in Figure 2.

that this behavior illustrates the need to account simultaneously for redox reactions and EDL formation and to determine the concentration of each species in the electrodes and in the electrolyte during the entire cycle. Indeed, previous models[37,39,40,44,46] assumed constant and uniform ion concentrations in the electrodes and electrolyte when simulating faradaic reactions. The present results indicate that such assumptions may be valid for parts of the cycle but not for others. Then, diffusion limitations or reactant starvation cannot be accounted for while they play an important role in the energy storage mechanisms. In addition, in both Cases A and B, the state of charge or the Li saturation $c_{1,P}/c_{1,P,max}$ was very small. This justifies the assumption of perfect faradaic behavior characterized by $\Delta\psi_{eq} = 0$ V.

Overall, Case B featured two regimes: a faradaic regime and a capacitive regime. Note that the faradaic regime is desirable because it results in larger total current and capacitance. Indeed, the integral areal capacitance $C_{s,int}$ was 47.9 μF/cm^2 in Case A at 1 V/s when the current was exclusively faradaic. This was almost double the capacitance of 24.8 μF/cm^2 achieved by the device simulated in Case B, also at 1 V/s. To further elucidate these regimes, it is worth considering the temporal variation of other important variables.

Figure 3 shows the temporal evolution of (a) the faradaic j_F and capacitive j_C current densities, (b) the overpotential $\eta(t)$, (c) the exchange current density $j_{F,0}(t)$, and (d) the ion concentrations of Li^+ $c_1(-L+H,t)$ and of ClO_4^- $c_2(-L + H,t)$ at the Stern/diffuse layer interface as functions of dimensionless time t/τ_{CV} for Case B at scan rate $v = 1$ V/s. Figure 3a clearly shows the two prevailing regimes. A dominant capacitive current was observed at the beginning of the charging step for $t/\tau_{CV} < 0.3$ and during part of the discharging step for $t/\tau_{CV} > 0.65$. This corresponded to 0.8 V > ψ_s > −0.3 V encompassing charging and discharging. A dominant faradaic current prevailed for t/τ_{CV} between 0.3 and 0.65 across the charging/discharging transition corresponding to −0.8 V < ψ_s < −0.3 V.

Figure 3b shows that the overpotential $\eta(t)$ varied linearly with a large slope during the capacitive regime and a smaller slope around $\eta = 0$ V during the faradaic regime. Indeed, in the case of $\Delta\psi_{eq} = 0$ V, $\eta(t)$ is such that $\eta(t)/H = \Delta\psi_H/H \approx \partial\psi/\partial x(-L + H,t)$. Then, combining this expression with the expression of $j_C(t)$ given by eq 16 yields $\partial\eta/\partial t \approx j_C(t)H/\epsilon_0\epsilon_r$. Thus, the time rate of change of $\eta(t)$ depends on the value of

DOI: 10.1021/acs.jpcc.5b00641
J. Phys. Chem. C 2015, 119, 11349−11361

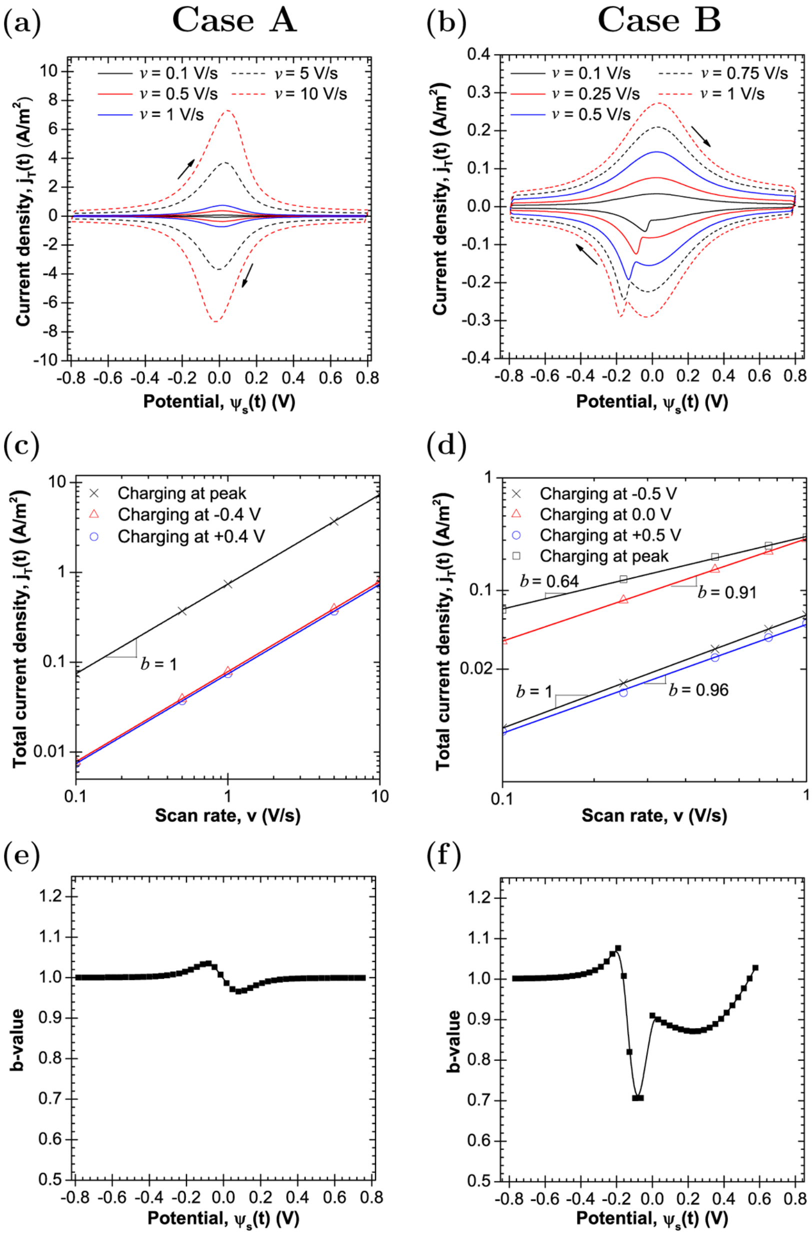

Figure 4. CV curves for multiple scan rates for (a) Case A and (b) Case B. Total current density j_T as a function of scan rate v in log scale for a selection of imposed potentials $\psi_s(t)$ for (c) Case A and (d) Case B. Computed b-value as a function of imposed potential $\psi_s(t)$ for (e) Case A and (f) Case B using the charging current for all scan rates shown in panels a and b, respectively. The regression coefficient R^2 obtained in the fitting of the b-value was larger than 0.95 for all values of ψ_s.

the capacitive current $j_C(t)$. The latter is significant during the capacitive regime and very small during the faradaic regime. This explains the large differences in slopes of $\eta(t)$ in the two regimes shown in Figure 3b.

Figure 3c shows the exchange current density $j_{F,0}(t)$ computed from the concentrations of Li$^+$ at the Stern/diffuse layer interface $c_1(-L + H,t)$ and of Li at the pseudocapacitive electrode/electrolyte interface $c_{1,P}(-L,t)$, according to eq 18. During the capacitive regime, the exchange current density was negligibly small. This was due to the fact that $c_{1,P}(-L,t)$ was nearly zero during this regime (Figure 2d). It explains why the faradaic current $j_F(t)$ was small despite the large overpotential $\eta(t)$ (Figure 3b). Similarly, during the faradaic regime, $j_{F,0}(t)$ was large resulting in large faradaic current $j_F(t)$ despite the small overpotential $\eta(t)$. Notably, during the discharging step $c_{1,P}(-L,t)$ reached zero at dimensionless time t/τ_{CV} = 0.65 corresponding to $\psi_s = -0.3$ V (blue square). This corresponded to (i) a vanishing exchange current density $j_{F,0}$, (ii) the start of the sharp decrease in the faradaic current $j_F(t)$ around $\psi_s = -0.3$ V, (iii) the onset of the EDL formation (Figure 3d), and (iv) the associated capacitive current (Figure 3a). This confirms that the lack of lithium atoms at the electrode surface was the cause of the transition from the faradaic to the capacitive regime corresponding to a switch in the charge storage mechanism observed in the CV curve around −0.3 V during discharging shown in Figure 2c (blue square). Then, the faradaic current was limited by out-diffusion (or deintercalation) of intercalated Li in the electrode.

Similarly, Figure 3d also displays the two distinct regimes in the Li$^+$ and ClO$_4^-$ concentrations at the Stern/diffuse layer interface. During the faradaic regime, both ion concentrations remained constant and nearly equal to the bulk concentration, i.e., $c_1(-L + H,t) = c_2(-L + H,t) \approx c_{1,\infty} = c_{2,\infty} = 1$ mol/L. This indicates that the redox reaction was fast enough to consume any excess Li^+ at the interface, while ion diffusion in the electrolyte was sufficiently fast to replenish the ions consumed by the reaction and available in large amounts in the relatively large electrolyte domain. Therefore, during this regime, the contribution of the capacitive current j_C to the total current j_T was negligible. By contrast, during the capacitive regime, the anion ClO_4^- formed an EDL near the pseudocapacitive electrode surface resulting in a significant capacitive current (Figure 3a). Indeed, in the capacitive regime, the overpotential $\eta(t)$ was positive so that the electric field attracted the negatively charged anions electrostatically to the electrode surface. In fact, $c_2(-L + H,t)$ quickly reached its maximum value $c_{2,max} = 1/N_A\ a_2^3$. The saturation of the electrode surface with ClO_4^- ions caused the capacitive current to reach a maximum around $t/\tau_{CV} = 0.8$ (Figure 3a) and was responsible for the hump observed in the CV curve at $\psi_s = 0$ V in the discharging step (Figure 2b). Note that similar observations were made in CV curves of EDLCs.[81]

Finally, Figure 3a shows that the faradaic current remained positive, corresponding to deintercalation of Li, during most of the charging step. The late reversal of the faradaic current was due to the fact that $j_F(t)$ always has the same sign as $\eta(t)$ [eq 17]. Therefore, $\eta(t)$ had to become negative for the faradaic current to change sign. However, Figure 3b shows that, in the capacitive regime during the discharging step, the overpotential increased due to the formation of the EDL by the anion ClO_4^- at the electrode surface. This EDL had to dissolve before the overpotential became negative and the faradaic current reversed sign. Figure 3d confirms that the onset of the faradaic regime coincided with the complete dissolution of the ClO_4^- EDL, while the concentration of Li^+ $c_1(-L + H,t)$ at the Stern/diffuse layer interface increased from zero to $c_{1,\infty}$. As a consequence, the formation of a thick EDL of ClO_4^- ions in the capacitive regime during the discharging step causes the late onset of the faradaic current during the charging step. Therefore, preventing or delaying the capacitive regime during discharging would also increase the length of the faradaic regime during charging.

Analysis of the *b*-Value. Figure 4a,b shows the numerically predicted CV curves for scan rates v ranging from 0.1 to 10 V/s for Cases A and B, respectively. Figure 4a indicates that, in the case of a thin electrode with fast intercalation (Case A), the CV curves were similar in shape with the total current density $j_T(\psi_s)$ increasing with scan rate. This suggests that the cell was not limited by diffusion of any species for the range of scan rates considered. Figure 4b shows similar CV curves for different scan rates in the case of a thick electrode with slow intercalation corresponding to Case B. The peaks and humps apparent during charging shifted to lower potential ψ_s as the scan rate v increased. Note that this was consistent with experimental observations of Li^+ insertion in nanocrystalline films of orthorhombic Nb_2O_5[7] or in TiO_2 anatase.[14] Here also, the total current j_T achieved in Case B was much smaller than that observed in Case A, for any given scan rate v and potential ψ_s. In other words, the capacitance of the thin electrode with fast intercalation (Case A) was much larger than that of the thick electrode with slow intercalation (Case B).

Figure 4c,d shows the total current density $j_T(t)$ during charging as a function of scan rate v in log scale for different values of potential $\psi_s(t)$ for Cases A and B, respectively. Figure 4c shows that, for Case A, the total current j_T increased linearly with scan rate v for $\psi_s = -0.4$ V and +0.4 V. The same observation was made for all potentials across the potential window including the current at the charging peak, also known as cathodic peak. However, Figure 4d indicates that, for Case B, the evolution of the total current density $j_T(t)$ with the scan rate v depended on the potential considered. The *b*-value was equal to (i) 1 for $\psi_s = -0.5$ V, when the current was exclusively faradaic, (ii) 0.96 for $\psi_s = 0.5$ V when the total current was exclusively capacitive, and (iii) 0.91 for $\psi_s = 0$ V when the total current was a combination of faradaic and capacitive contributions. In addition, the current at the charging peak evolved as $j_{T,pa} \propto v^{0.64}$. This decrease in the *b*-value around the peak associated with the faradaic process was consistent with experimental observations for both two- and three-electrode experiments.[7,18,22,25−27,29] As discussed earlier, the charging peak, corresponding to the lowest *b*-value, was located at the transition between the faradaic and capacitive regimes, as shown in Figure 2c.

Figure 4e,f shows the *b*-value as a function of the potential ψ_s computed by the least-squares method from the total current density j_T vs scan rate v shown in Figure 4c,d for Cases A and B, respectively. Figure 4e indicates that for Case A the *b*-value was independent of ψ_s and close to unity across the potential window. Note that the faradaic current with fast intercalation dominated for all potentials (Figure 2a). Thus, these results indicate that a *b*-value of unity can be associated with fast reversible faradaic reaction in thin electrodes. Then, the faradaic current j_F was proportional to the scan rate v, as also observed in EDLCs. Thus, this behavior can be referred to as "capacitive behavior". However, the charge storage mechanism is truly faradaic and not capacitive. By contrast, for Case B, Figure 4f indicates that the *b*-value featured a drop from 1 to about 0.6, as often observed in experimental studies of pseudocapacitors.[14,25,83] In fact, it is interesting to note that Figure 4f is analogous to Figure 10c of ref 22 obtained experimentally with a two-electrode cell with a working electrode made of anatase TiO_2 and a counter electrode made of lithium metal with 1 mol/L $LiPF_6$ in a 1:1 ethylene carbonate and dimethyl carbonate mixture as electrolyte.[22] Similar results were also reported in Figure 5 of ref 25 obtained experimentally in a three-electrode experiment with a working electrode made of nanocrystalline anatase TiO_2 nanoparticles deposited on glassy carbon with 1 mol/L $LiClO_4$ salt in PC as electrolyte and lithium metal for both the counter and the reference electrodes.[25]

The dip in the *b*-value has often been attributed to the intercalation process on the basis that $j_T \propto v^{1/2}$ for reversible redox reactions with semi-infinite diffusion of the reaction products and in the absence of electric double layers, as previously discussed.[13] However, the dip in the *b*-value predicted numerically did not occur during the faradaic regime but for $-0.2\ V < \psi_s < 0$ V corresponding to the transition between the capacitive and faradaic regimes (Figure 2c). Previous models accounting separately for redox reactions and for electric double layer[37−46] would not be able to predict the dip in the *b*-value caused by the interplay between the two phenomena requiring the prediction of the concentrations of all species in the entire domain to account for reactant starvation. For larger potentials, $\psi_s > 0$ V, the *b*-value increased again to a value close to unity. In this region, the capacitive current dominated, and the *b*-value was consistent with the expression of capacitive current evolution with the scan rate given by $j_C = C_s v$ where C_s is the areal capacitance.[13,15]

CONCLUSION

This article presented a new physicochemical model, derived from first-principles, for hybrid supercapacitors featuring a pseudocapacitive electrode and a carbon electrode subjected to cyclic voltammetry. The model simultaneously accounted for (i) charge transport in both electrodes and electrolytes, (ii) the dynamics of the electric double layer, (iii) steric repulsion due to finite ion sizes, (iv) redox reactions, and (v) intercalation. The results showed that for fast intercalation in a thin electrode the current was always due to the faradaic reaction and that the *b*-value was unity across the potential window. For relatively thick electrodes and slow intercalation, the CV curves exhibited two distinct regimes. First, a faradaic regime prevailed for the more negative potentials and was dominated by the faradaic reaction and limited mainly by the diffusion of Li in the pseudocapacitive electrode during discharge. Second, a capacitive regime dominated at larger potentials with current due to the formation of an EDL at the electrode surface. A *b*-value of unity was associated with both regimes. The dip in *b*-value, often observed experimentally,[18,25,28] was shown to occur during the transition between these two regimes.

ASSOCIATED CONTENT

Supporting Information

Results for concentration-dependent ion diffusion coefficients and effect of variable equilibrium potential difference on the current magnitude and the *b*-value. The Supporting Information is available free of charge on the ACS Publications website at DOI: 10.1021/acs.jpcc.5b00641.

AUTHOR INFORMATION

Corresponding Author

*Phone: +1 (310) 206-5598. Fax: +1 (310) 206-2302. E-mail: pilon@seas.ucla.edu.

Notes

The authors declare no competing financial interest.

ACKNOWLEDGMENTS

This material is based upon work supported as part of the Molecularly Engineered Energy Materials, an Energy Frontier Research Center funded by the U.S. Department of Energy, Office of Science, Office of Basic Energy Sciences under Award Number DE-SC0001342.

NOMENCLATURE

a	effective ion diameter (nm)
b	*b*-value, power constant in $j_t = av^b$
c	ion concentration (mol/L)
c_{max}	maximum ion concentration, $c_{max} = 1/N_A a^3$ (mol/L)
$C_{s,int}$	integral areal capacitance (F/m^2)
$c_{1,P,0}$	initial concentration of intercalated Li in the pseudocapacitive electrode (mol/L)
$c_{1,P,max}$	maximum concentration of intercalated Li, $c_{1,P,max} = m\rho/M$ (mol/L)
D	diffusion coefficient of ions in electrolyte (m^2/s)
$D_{1,P}$	diffusion coefficient of intercalated Li in the pseudocapacitive electrode (m^2/s)
e	elementary charge, $e = 1.602 \times 10^{-19}$ C
F	Faraday constant, $F = e\ N_A = 9.648 \times 10^4$ C mol^{-1}
H	Stern layer thickness (nm)
j_C	predicted capacitive current density (A/m^2)
j_F	predicted faradaic current density (A/m^2)
j_T	predicted total current density (A/m^2)
k_0	reaction rate constant, eq 18 (m$^{2.5}$ mol$^{-0.5}$ s^{-1})
L	half of interelectrode distance (nm)
L_C	thickness of the carbon electrode (nm)
L_P	thickness of the pseudocapacitive electrode (nm)
m	stoichiometric number of intercalated Li, $Li_mM_pO_q$
M	molecular weight of the fully intercalated active electrode material (g/mol)
n	index of refraction of the electrolyte
n_c	cycle number
N_A	Avogadro constant, $N_A = 6.022 \times 10^{23}$ mol^{-1}
N_i	ion flux of species i (mol m^{-2} s^{-1})
p,q	stoichiometric numbers of the metal and oxygen in the metal oxide M_pO_q
R_u	universal gas constant, $R_u = 8.314$ J mol^{-1} K^{-1}
T	local temperature (K)
t	time (s)
v	scan rate of the cyclic voltammetry (V/s)
x	location in one-dimensional space (μm)
z	ion valency

GREEK SYMBOLS

α	transfer coefficient, eqs 17 and 18
β	fitting parameter for the Booth Model, eq 23
ϵ_0	vacuum permittivity, $\epsilon_0 = 8.854 \times 10^{-12}$ F m^{-1}
ϵ_r	relative permittivity of electrolyte
$\Delta\psi_{eq}$	equilibrium potential difference (V)
$\Delta\psi_H$	potential drop across the Stern layer (V)
λ_D	Debye length (m)
η	overpotential, $\eta = \Delta\psi_H - \Delta\psi_{eq}$ (V)
ρ	density of the fully intercalated pseudocapacitive electrode material (kg/m^3)
σ	electrical conductivity of electrode (S/m)
τ_{CV}	cycle period (s)
ψ	electric potential (V)
ψ_{min}, ψ_{max}	minimum and maximum of the potential window (V)
ψ_s	imposed cell potential (V)

SUBSCRIPTS

∞	refers to bulk electrolyte
i	refers to ion species i
C	refers to the carbon electrode
P	refers to the pseudocapacitive electrode

REFERENCES

(1) US Department of Energy. *Basic Research Needs for Electrical Energy Storage*, 2007. http://www.osti.gov/accomplishments/documents/fullText/ACC0330.pdf.

(2) Simon, P.; Gogotsi, Y. Materials for Electrochemical Capacitors. *Nat. Mater.* **2008**, *7*, 845−854.

(3) Zhang, Y.; Feng, H.; Wu, X.; Wang, L.; Zhang, A.; Xia, T.; Dong, H.; Li, X.; Zhang, L. Progress of Electrochemical Capacitor Electrode Materials: a Review. *Int. J. Hydrogen Energy* **2009**, *34*, 4889−4899.

(4) Abbey, C.; Joos, G. Supercapacitor Energy Storage for Wind Energy Applications. *IEEE Trans. Ind. Appl.* **2007**, *43*, 769−776.

(5) Wu, Z.-S.; Zhou, G.; Yin, L.-C.; Ren, W.; Li, F.; Cheng, H.-M. Graphene/Metal Oxide Composite Electrode Materials for Energy Storage. *Nano Energy* **2012**, *1*, 107−131.

(6) Wang, G.; Zhang, L.; Zhang, J. A Review of Electrode Materials for Electrochemical Supercapacitors. *Chem. Soc. Rev.* **2012**, *41*, 797−828.

(7) Augustyn, V.; Come, J.; Lowe, M. A.; Kim, J. W.; Taberna, P.-L.; Tolbert, S. H.; Abruña, H. D.; Simon, P.; Dunn, B. High-Rate Electrochemical Energy Storage through Li$^+$ Intercalation Pseudocapacitance. *Nat. Mater.* **2013**, *12*, 518−522.

(8) Qu, Q.; Zhang, P.; Wang, B.; Chen, Y.; Tian, S.; Wu, Y.; Holze, R. Electrochemical Performance of MnO$_2$ Nanorods in Neutral Aqueous Electrolytes as a Cathode for Asymmetric Supercapacitors. *J. Phys. Chem. C* **2009**, *113*, 14020−14027.

(9) Long, J. W.; Bélanger, D.; Brousse, T.; Sugimoto, W.; Sassin, M. B.; Crosnier, O. Asymmetric Electrochemical Capacitors-Stretching the Limits of Aqueous Electrolytes. *MRS Bull.* **2011**, *36*, 513−522.

(10) Fan, Z.; Yan, J.; Wei, T.; Zhi, L.; Ning, G.; Li, T.; Wei, F. Asymmetric Supercapacitors Based on Graphene/MnO$_2$ and Activated Carbon Nanofiber Electrodes with High Power and Energy Density. *Adv. Funct. Mater.* **2011**, *21*, 2366−2375.

(11) Wang, F.; Xiao, S.; Hou, Y.; Hu, C.; Liu, L.; Wu, Y. Electrode Materials for Aqueous Asymmetric Supercapacitors. *RCS Adv.* **2013**, *3*, 13059−13084.

(12) Demarconnay, L.; Raymundo-Piñero, E.; Béguin, F. Adjustment of Electrodes Potential Window in an Asymmetric Carbon/MnO$_2$ Supercapacitor. *J. Power Sources* **2011**, *196*, 580−586.

(13) Bard, A. J.; Faulkner, L. R. *Electrochemical Methods: Fundamentals and Applications*; John Wiley & Sons: New York, 2001.

(14) Lindstrom, H.; Sodergren, S.; Solbrand, A.; Rensmo, H.; Hjelm, J.; Hagfeldt, A.; Lindquist, S. E. Li$^+$ Ion Insertion in TiO$_2$ (Anatase). 2. Voltammetry on Nanoporous Films. *J. Phys. Chem. B* **1997**, *101*, 7717−7722.

(15) Conway, B. E. *Electrochemical Supercapacitors: Scientific Fundamentals and Technological Applications*; Kluwer Academic/Plenum Publishers: New York, 1999.

(16) Wang, H.; Xu, Z.; Li, Z.; Cui, K.; Ding, J.; Kohandehghan, A.; Tan, X.; Zahiri, B.; Olsen, B. C.; Holt, C. M.; et al. Hybrid Device Employing Three-Dimensional Arrays of MnO in Carbon Nanosheets Bridges Battery-Supercapacitor Divide. *Nano Lett.* **2014**, *14*, 1987−1994.

(17) Li, S.; Qiu, J.; Lai, C.; Ling, M.; Zhao, H.; Zhang, S. Surface Capacitive Contributions: Towards High Rate Anode Materials for Sodium Ion Batteries. *Nano Energy* **2015**, *12*, 224−230.

(18) López, M. C.; Ortiz, G. F.; Lavela, P.; Alcántara, R.; Tirado, J. L. Improved Energy Storage Solution Based on Hybrid Oxide Materials. *ACS Sustainable Chem. Eng.* **2013**, *1*, 46−56.

(19) Chen, Z.; Wang, J. W.; Lu, C.; Liu, Z.; Chortos, N.; Pan, A.; Wei, L.; Cui, F.; Bao, Y.; Three-Dimensionally, Z. A. Interconnected Carbon Nanotube-Conducting Polymer Hydrogel Network for High-Performance Flexible Battery Electrodes. *Adv. Energy Mater.* **2014**, *4*, 1400207.

(20) Lim, E.; Kim, H.; Jo, C.; Chun, J.; Ku, K.; Kim, S.; Lee, H. I.; Nam, I.-S.; Yoon, S.; Kang, K.; et al. Advanced Hybrid Supercapacitor Based on a Mesoporous Niobium Pentoxide/Carbon as High-Performance Anode. *ACS Nano* **2014**, *8*, 8968−8978.

(21) Lin, Y.-M.; Abel, P. R.; Flaherty, D. W.; Wu, J.; Stevenson, K. J.; Heller, A.; Mullins, C. B. Morphology Dependence of the Lithium Storage Capability and Rate Performance of Amorphous TiO$_2$ Electrodes. *J. Phys. Chem. C* **2011**, *115*, 2585−2591.

(22) Zhao, B.; Shao, Z. From Paper to Paper-like Hierarchical Anatase TiO$_2$ Film Electrode for High-Performance Lithium-Ion Batteries. *J. Phys. Chem. C* **2012**, *116*, 17440−17447.

(23) Kim, J.-H.; Zhu, K.; Kim, J. Y.; Frank, A. J. Tailoring Oriented TiO$_2$ Nanotube Morphology for Improved Li Storage Kinetics. *Electrochim. Acta* **2013**, *88*, 123−128.

(24) Cheng, Q.; Liang, J.; Zhu, Y.; Si, L.; Guo, C.; Qian, Y. Bulk Ti$_2$Nb$_{10}$O$_{29}$ as Long-Life and High-Power Li-ion Battery Anodes. *J. Mater. Chem. A* **2014**, *2*, 17258−17262.

(25) Wang, J.; Polleux, J.; Lim, J.; Dunn, B. Pseudocapacitive Contributions to Electrochemical Energy Storage in TiO$_2$ (Anatase) Nanoparticles. *J. Phys. Chem. C* **2007**, *111*, 14925−14931.

(26) Brezesinski, T.; Wang, J.; Tolbert, S. H.; Dunn, B. Ordered Mesoporous α-MoO$_3$ with Iso-Oriented Nanocrystalline Walls for Thin-Film Pseudocapacitors. *Nat. Mater.* **2010**, *9*, 146−151.

(27) Wang, X.; Li, G.; Chen, Z.; Augustyn, V.; Ma, X.; Wang, G.; Dunn, B.; Lu, Y. High-Performance Supercapacitors Based on Nanocomposites of Nb$_2$O$_5$ Nanocrystals and Carbon Nanotubes. *Adv. Energy Mater.* **2011**, *1*, 1089−1093.

(28) Shao, L.; Jeon, J.-W.; Lutkenhaus, J. L. Porous Polyaniline Nanofiber/Vanadium Pentoxide Layer-by-Layer Electrodes for Energy Storage. *J. Mater. Chem. A* **2013**, *1*, 7648−7656.

(29) Abdur, R.; Kim, K.; Kim, J.-H.; Lee, J. Electrochemical Behavior of Manganese Oxides on Flexible Substrates for Thin Film Supercapacitors. *Electrochim. Acta* **2014**, *153*, 184−189.

(30) Gu, F.; Cheng, X.; Wang, S.; Wang, X.; Lee, P. S. Oxidative Intercalation for Monometallic Ni$_2^+$-Ni$_3^+$ Layered Double Hydroxide and Enhanced Capacitance in Exfoliated Nanosheets. *Small* **2014**, *11*, 2044−2050.

(31) Kong, L.; Zhang, C.; Zhang, S.; Wang, J.; Cai, R.; Lv, C.; Qiao, W.; Ling, L.; Long, D. High-Power and High-Energy Asymmetric Supercapacitors Based on Li$^+$-intercalation into a T-Nb$_2$O$_5$/Graphene Pseudocapacitive Electrode. *J. Mater. Chem. A* **2014**, *2*, 17962−17970.

(32) Li, J.; Tang, Z.; Zhang, Z. Pseudocapacitive Characteristic of Lithium Ion Storage in Hydrogen Titanate Nanotubes. *Chem. Phys. Lett.* **2006**, *418*, 506−510.

(33) Conway, B. E.; Birss, V.; Wojtowicz, J. The Role and Utilization of Pseudocapacitance for Energy Storage by Supercapacitors. *J. Power Sources* **1997**, *66*, 1−14.

(34) Guillemet, P.; Brousse, T.; Crosnier, O.; Dandeville, Y.; Athouel, L.; Scudeller, Y. Modeling Pseudo Capacitance of Manganese Dioxide. *Electrochim. Acta* **2012**, *67*, 41−49.

(35) Rubinson, J. F.; Kayinamura, Y. P. Charge Transport in Conducting Polymers: Insights from Impedance Spectroscopy. *Chem. Soc. Rev.* **2009**, *38*, 3339−3347.

(36) Bazant, M. Z.; Thornton, K.; Ajdari, A. Diffuse-Charge Dynamics in Electrochemical Systems. *Phys. Rev. E* **2004**, *70*, 021506.

(37) Lin, C.; Ritter, J. A.; Popov, B. N.; White, R. E. A Mathematical Model of an Electrochemical Capacitor with Double-Layer and Faradaic Processes. *J. Electrochem. Soc.* **1999**, *146*, 3168−3175.

(38) Lin, C.; Popov, B. N.; Ploehn, H. J. Modeling the Effects of Electrode Composition and Pore Structure on the Performance of Electrochemical Capacitors. *J. Electrochem. Soc.* **2002**, *149*, A167−A175.

(39) Farsi, H.; Gobal, F. A Mathematical Model of Nanoparticulate Mixed Oxide Pseudocapacitors; Part II: the Effects of Intrinsic Factors. *J. Solid State Electrochem.* **2011**, *15*, 115−123.

(40) Kadyk, T.; Eikerling, M. Charging Mechanism and Moving Reaction Fronts in a Supercapacitor with Pseudocapacitance. *J. Electrochem. Soc.* **2014**, *161*, A239−A246.

(41) Pillay, B. *Design of Electrochemical Capacitors for Energy Storage.* Ph.D. Thesis, Deptartment of Chemical Engineering, University of California, Berkeley, CA, 1996.

(42) Kim, H.; Popov, B. N. A Mathematical Model of Oxide, Carbon Composite Electrode for Supercapacitors. *J. Electrochem. Soc.* **2003**, *150*, 1153−1160.

(43) Somasundaram, K.; Birgersson, E.; Mujumdar, A. S. Analysis of a Model for an Electrochemical Capacitor. *J. Electrochem. Soc.* **2011**, *158*, 1220−1230.

(44) Staser, J. A.; Weidner, J. W. Mathematical Modeling of Hybrid Asymmetric Electrochemical Capacitors. *J. Electrochem. Soc.* **2014**, *161*, E3267−E3275.

(45) Sikha, G.; White, R. E.; Popov, B. N. A Mathematical Model for a Lithium-ion Battery/Electrochemical Capacitor Hybrid System. *J. Electrochem. Soc.* **2005**, *152*, A1682−A1693.

(46) Devan, S.; Subramanian, V. R.; White, R. E. Transient Analysis of a Porous Electrode. *J. Electrochem. Soc.* **2005**, *152*, 947−955.

(47) Bazant, M. Z.; Kilic, M. S.; Storey, B. D.; Ajdari, A. Towards an Understanding of Induced-Charge Electrokinetics at Large Applied Voltages in Concentrated Solutions. Adv. Colloid Electrochem. Soc. *Interface Sci.* **2009**, *152*, 48−88.

(48) Liu, Y.; Zhou, F.; Ozolins, V. *Ab Initio* Study of the Charge-Storage Mechanisms in RuO_2-Based Electrochemical Ultracapacitors. *J. Phys. Chem. C* **2012**, *116*, 1450−1457.

(49) Ozolins, V.; Zhou, F.; Asta, M. Ruthenia-Based Electrochemical Supercapacitors: Insights from First-Principles Calculations. *Acc. Chem. Res.* **2013**, *46*, 1084−1093.

(50) Kang, J.; Wei, S.-H.; Zhu, K.; Kim, Y.-H. First-Principles Theory of Electrochemical Capacitance of Nanostructured Materials: Dipole-Assisted Subsurface Intercalation of Lithium in Pseudocapacitive TiO_2 Anatase Nanosheets. *J. Phys. Chem. C* **2011**, *115*, 4909−4915.

(51) Tompsett, D. A.; Parker, S. C.; Bruce, P. G.; Islam, M. S. Nanostructuring of β-MnO_2: The Important Role of Surface to Bulk Ion Migration. *Chem. Mater.* **2013**, *25*, 536−541.

(52) Ding, H.; Ray, K. G.; Ozolins, V.; Asta, M. Structural and Vibrational Properties of α-MoO_3 from Van der Waals Corrected Density Functional Theory Calculations. *Phys. Rev. B* **2012**, *85*, 012104.

(53) Feng, G.; Cummings, P. T. Supercapacitor Capacitance Exhibits Oscillatory Behavior as a Function of Nanopore Size. J. *Phys. Chem. Lett.* **2011**, *2*, 2859−2864.

(54) He, Y.; Huang, J.; Sumpter, B. G.; Kornyshev, A. A.; Qiao, R. Dynamic Charge Storage in Ionic Liquids-filled Nanopores: Insight from a Computational Cyclic Voltammetry Study. *J. Phys. Chem. Lett.* **2015**, *6*, 22−30.

(55) Wang, H.; Pilon, L. Accurate Simulations of Electric Double Layer Capacitance of Ultramicroelectrodes. *J. Phys. Chem. C* **2011**, *115*, 16711−16719.

(56) Wang, H.; Thiele, A.; Pilon, L. Simulations of Cyclic Voltammetry For Electric Double Layers In Asymmetric Electrolytes: A Generalized Modified Poisson-Nernst-Planck Model. *J. Phys. Chem. C* **2013**, *117*, 18286−18297.

(57) Masliyah, J. H., Bhattacharjee, S. *Electrokinetic and Colloid Transport Phenomena*; John Wiley & Sons: New York, 2006.

(58) Merlet, C.; Salanne, M.; Rotenberg, B.; Madden, P. A. Influence of Solvation on the Structural and Capacitive Properties of Electrical Double Layer Capacitors. *Electrochim. Acta* **2013**, *101*, 262−271.

(59) Umino, S.; Newman, J. Diffusion of Sulfuric Acid in Concentrated Solutions. *J. Electrochem. Soc.* **1993**, *140*, 2217−2221.

(60) Come, J.; Augustyn, V.; Kim, J. W.; Rozier, P.; Taberna, P.-L.; Gogotsi, P.; Long, J. W.; Dunn, B.; Simon, P. Electrochemical Kinetics of Nanostructured Nb_2O_5 Electrodes. *J. Electrochem. Soc.* **2014**, *161*, A718−A725.

(61) Wang, H.; Varghese, J.; Pilon, L. Simulation of Electric Double Layer Capacitors with Mesoporous Electrodes: Effects of Morphology and Electrolyte Permittivity. *Electrochim. Acta* **2011**, *56*, 6189−6197.

(62) Wang, H.; Pilon, L. Mesoscale Modeling of Electric Double Layer Capacitors with Three-Dimensional Ordered Structures. *J. Power Sources* **2013**, *221*, 252−260.

(63) Goldin, G. M.; Colclasure, A. M.; Wiedemann, A. H.; Kee, R. J. Three-Dimensional Particle-Resolved Models of Li-ion Batteries to Assist the Evaluation of Empirical Parameters in One-Dimensional Models. *Electrochim. Acta* **2012**, *64*, 118−129.

(64) Wang, C.; Sastry, A. M. Mesoscale Modeling of a Li-Ion Polymer Cell. *J. Electrochem. Soc.* **2007**, *154*, 1035−1047.

(65) Subramanian, S. R.; Boovaragavan, V.; Ramadesigan, V.; Arabandi, M. Mathematical Model Reformulation for Lithium-Ion Battery Simulations: Galvanostatic Boundary Conditions. *J. Electrochem. Soc.* **2009**, *156*, 260−271.

(66) Cohen, H.; Cooley, J. W. The Numerical Solution of the Time-Dependent Nernst-Planck Equations. *Biophys. J.* **1965**, *5*, 145−162.

(67) Jow, T.; Zheng, J. Electrochemical Capacitors Using Hydrous Ruthenium Oxide and Hydrogen Inserted Ruthenium Oxide. *J. Electrochem. Soc.* **1998**, *145*, 49−52.

(68) Cottineau, T.; Toupin, M.; Delahaye, T.; Brousse, T.; Bélanger, D. Nanostructured Transition Metal Oxides for Aqueous Hybrid Electrochemical Supercapacitors. *Appl. Phys. A: Mater. Sci. Process.* **2006**, *82*, 599−606.

(69) Khomenko, V.; Raymundo-Piñero, E.; Béguin, F. Optimisation of an Asymmetric Manganese Oxide/Activated Carbon Capacitor Working at 2V in Aqueous Medium. *J. Power Sources* **2006**, *153*, 183−190.

(70) Booth, F. The Dielectric Constant of Water and the Saturation Effect. *J. Chem. Phys.* **1951**, *19*, 391−394.

(71) Appleby, A. *In Modern Aspects of Electrochemistry*; Conway, B. E., Vayenas, C. G., White, R. E., Gamboa-Adelco, M. E., Eds.; Springer: New York, 2005; pp 175−301.

(72) Nishikaw, K.; Fukunaka, Y.; Sakka, T.; Ogata, Y. H.; Selman, J. R. Measurement of $LiClO_4$ Diffusion Coefficient in Propylene Carbonate by Moire Pattern. *J. Electrochem. Soc.* **2006**, *153*, 830−834.

(73) Lin, Y.-P.; Wu, N.-L. Characterization of $MnFe_2O_4$/$LiMn_2O_4$ Aqueous Asymmetric Supercapacitor. *J. Power Sources* **2011**, *196*, 851−854.

(74) Aguirre, J. C.; Ferreira, A.; Ding, H.; Jenekhe, S. A.; Kopidakis, N.; Asta, M.; Pilon, L.; Rubin, Y.; Tolbert, S. H.; Schwartz, B. J.; et al. Panoramic View of Electrochemical Pseudocapacitor and Organic Solar Cell Research in Molecularly Engineered Energy Materials (MEEM). *J. Phys. Chem. C* **2014**, *118*, 19505−19523.

(75) Bosman, A.; Crevecoeur, C. Mechanism of the Electrical Conduction in Li-Doped NiO. *Phys. Rev.* **1966**, *144*, 763.

(76) Bélanger, D.; Brousse, T.; Long, J. W. Manganese Oxides: Battery Materials Make the Leap to Electrochemical Capacitors. *Electrochem. Soc. Interface* **2008**, *17*, 49−52.

(77) Zhang, L. L.; Zhou, R.; Zhao, X. S. Graphene-Based Materials as Supercapacitor Electrodes. *J. Mater. Chem.* **2010**, *20*, 5983−5992.

(78) Colclasure, A. M.; Kee, R. J. Thermodynamically Consistent Modeling of Elementary Electrochemistry in Lithium-ion Batteries. *Electrochim. Acta* **2010**, *55*, 8960−8973.

(79) He, R.; Chen, S.; Yang, F.; Wu, B. Dynamic Diffuse Double-Layer Model for the Electrochemistry of Nanometer-Sized Electrodes. *J. Phys. Chem. B* **2006**, *110*, 3262−3270.

(80) Toupin, M.; Brousse, T.; Bélanger, D. Charge Storage Mechanism of MnO_2 Electrode Used in Aqueous Electrochemical Capacitor. *Chem. Mater.* **2004**, *16*, 3184−3190.

(81) Wang, H.; Pilon, L. Physical Interpretation of Cyclic Voltammetry for Measuring Electric Double Layer Capacitances. *Electrochim. Acta* **2012**, *64*, 130−139.

(82) Zhu, J.; Tang, S.; Xie, H.; Dai, Y.; Meng, X. Hierarchically Porous MnO2Microspheres Doped with Homogeneously Distributed Fe3O4 Nanoparticles for Supercapacitors. *ACS Appl. Mater. Interfaces* **2014**, *6*, 17637−17646.

(83) Zukalova, M.; Kalbac, M.; Kavan, L.; Exnar, I.; Graetzel, M. Pseudocapacitive Lithium Storage in TiO_2 (B). *Chem. Mater.* **2005**, *17*, 1248−1255.

DOI: 10.1021/acs.jpcc.5b00641